Dynamics of Atmospheres and Oceans 110 (2025) 101552

Contents lists available at ScienceDirect

Dynamics of Atmospheres and Oceans

journal homepage: www.elsevier.com/locate/dynatmoce

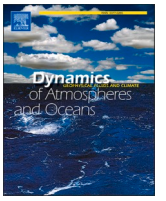

Sensitive area in the tropical Indian Ocean for advancing beyond the summer predictability barrier of Indian Ocean Dipole

Rong Feng [a,b], Wansuo Duan [a,c,*]

[a] State Key Laboratory of Earth System Numerical Modeling and Application, Institute of Atmospheric Physics, Chinese Academy of Sciences, Beijing 100029, China
[b] Shanghai Frontiers Science Center of Atmosphere-Ocean Interaction, Shanghai 200438, China
[c] College of Marine Sciences, University of Chinese Academy of Sciences, Qingdao 266400, China

ARTICLE INFO

Keywords:
Initial errors
Indian Ocean Dipole
Summer predictability barrier
Sensitive area
Targeted observations

ABSTRACT

Using the geophysical fluid dynamics laboratory climate model version 2p1 (GFDL CM2p1), perfect model predictability experiments have been conducted to identify the sensitive area in the tropical Indian Ocean for advancing beyond the summer predictability barrier (SPB) of positive Indian Ocean Dipole (IOD) events. In these experiments, the model is assumed to be perfect, and prediction errors are only caused by initial errors. Initially, the impact of initial error patterns on prediction uncertainties was assessed by comparing dipole pattern initial errors with three sets of spatially correlated noises. The results revealed that dipole pattern initial errors tend to result in larger prediction errors and higher error growth rates in summer, leading to a significant SPB phenomenon. Notably, the large values of these dipole pattern initial errors are concentrated in specific areas. By eliminating initial errors within these areas, the prediction errors in summer are largely reduced, underscoring the sensitivity of prediction uncertainties in summer to initial errors in these areas. Moreover, the prediction errors in summer exhibit a higher sensitivity to initial errors within the subsurface large value area compared to those within the surface large value area. Consequently, the subsurface large value area in the tropical Indian Ocean is the sensitive area for advancing beyond the SPB, aligning with the corresponding location for advancing beyond the WPB. Eliminating initial errors within this area leads to a rapid decrease in prediction uncertainties, with a more pronounced reduction in winter than in summer. Through intensive observations in this sensitive area, significant reductions in prediction errors in both summer and winter can be achieved, thereby greatly improve the forecast skill of IOD events.

1. Introduction

The Indian Ocean Dipole (IOD) is an important coupled ocean-atmosphere phenomenon in the tropical Indian Ocean, characterized by an east-west seesaw pattern of sea surface temperature anomalies (SSTAs), accompanied by anomalous wind fields in the equatorial region (Saji et al., 1999; Webster et al., 1999). This dipole-type oscillation is evident in both the surface and subsurface sea temperature anomalies (Feng and Meyers, 2003; Guo et al., 2015; Li et al., 2003). Seasonal phase-locking is an important characteristic of IOD events. Previous studies have pointed out that IOD events often reverse their sign in winter, rapidly develop in summer, peak in

* Corresponding author at: State Key Laboratory of Earth System Numerical Modeling and Application, Institute of Atmospheric Physics, Chinese Academy of Sciences, Beijing 100029, China.
E-mail address: duanws@lasg.iap.ac.cn (W. Duan).

https://doi.org/10.1016/j.dynatmoce.2025.101552
Received 3 September 2024; Received in revised form 8 December 2024; Accepted 1 April 2025
Available online 3 April 2025

autumn, and then quickly weaken and disappear in the following winter (Behera et al., 2006; Cai et al., 2005; Li et al., 2003; Saji et al., 1999; Wajsowicz, 2004; Webster et al., 1999). During positive IOD events, severe droughts often occur in the eastern Indian Ocean, Indonesia, and Australia, while there is excess rainfall in the western Indian Ocean and East Africa (Li et al., 2021; Wang and Cai, 2020). Furthermore, IOD events also impact weather and climate in other regions globally through the propagation of planetary waves (Duan et al., 2020; Yuan et al., 2008). Studies have shown that positive IOD events often lead to a weakening of the East Asian summer monsoon, strengthening of the South China Sea summer monsoon, increased precipitation in most parts of China, and extremely hot and dry conditions in southern regions during summer; the climate impacts of negative IOD events are generally the opposite (Qiu et al., 2014; Xiao et al., 2020; Yang et al., 2010). With global warming, the frequency of anomalies in the tropical Indian Ocean and IOD events is increasing, with a higher occurrence of strong IOD events (Cai et al., 2020; Huang et al., 2019; Hui and Zheng, 2018).

Based on the successful experiences of predictability research on the El Niño Southern Oscillation (ENSO), many scholars have conducted predictability studies on IOD events using numerical models (Du et al., 2020; Lu et al., 2018; Luo et al., 2007; Shi et al., 2012; Yuan et al., 2017; Zhu et al., 2015). Wajsowicz (2005) conducted ensemble retrospective experiments to evaluate the forecast skill of National Centers for Environmental Prediction Coupled Forecast System (NCEP CFS) in predicting the SSTAs in the eastern and western poles of IOD events. The study revealed that the forecast system is capable of predicting the SSTAs in the eastern pole up to 3–4 months in advance and in the western pole up to 6–7 months in advance. Shi et al. (2012) evaluated the forecast skills of four different prediction systems for the Indian Ocean SST. They found that the models can predict the IOD events about one season in advance, and for strong IOD events, this lead time can extend to two seasons. Luo et al. (2007) conducted an ensemble retrospective experiment on IOD events over the past 20 years using the Scale Interaction Experiment-Frontier Research Center for Global Change (SINTEX-F) model, which showed that the model could only predict IOD events 3–4 months in advance, and the forecast skill rapidly decreased when bestriding winter, leading to a winter predictability barrier (WPB) phenomenon. Therefore, most numerical models can only predict IOD events with a lead time of about one season (Luo et al., 2007; Shi et al., 2012; Zhu et al., 2015).

The possible reasons for the low forecast skill of IOD events mainly include the following aspects. Firstly, IOD events are influenced by complex physical processes, such as the strong Indian/Asian monsoon, interaction between IOD and ENSO, random intraseasonal oscillations in the atmosphere and ocean. Secondly, most numerical models currently cannot accurately describe the basic characteristics of IOD events, leading to model errors. Furthermore, although an Indian Ocean Observing System (IndOOS) has been established in the tropical Indian Ocean, observational data is sparse. Assimilating these observational data into models will introduce initial errors in the initial analysis fields. Feng et al. (2017) and Feng & Duan (2019) pointed out that initial sea temperature errors in the tropical Indian Ocean result in both the WPB and summer predictability barrier (SPB) phenomena. Liu et al. (2018) further analyzed the influence of initial sea temperature errors in the tropical Pacific Ocean on IOD predictability and revealed that a dipole mode-structured initial sea temperature errors most likely lead to the occurrence of the SPB phenomenon. The predictability barriers refer to a phenomenon that forecast skills rapidly decline when bestriding a specific season, regardless of the starting month (Luo et al., 2007). The existence of the WPB and SPB severely limits the forecast skill of IOD events.

As mentioned earlier, the current observational network in tropical oceans, especially in the tropical Indian Ocean, is sparse. There is a need to increase observations to enhance the accuracy of initial fields, which will reduce initial errors and improve the forecast skill of IOD events. However, conducting extensive observations comes with a substantial economic cost. Therefore, if similar effects can be achieved through observations in a smaller area, it can improve forecast skills while lowering economic costs. Consequently, the concept of targeted observations has gained widespread attention and application. Targeted observations aim to maximize the forecast skill of a specific region (verification area) at a future time (verification time) by increasing observations in a sensitive area at a specific time (target observation time) before the verification time using certain methods. The key to targeted observation approach is identifying the sensitive area for additional observations. Internationally, there are two categories of methods for exploring sensitive areas: adjoint-based methods, which involve calculating the adjoints of the forward tangent propagator of models, such as singular vectors (SVs; Palmer et al., 1998) and conditional nonlinear optimal perturbation (CNOP; Mu and Duan, 2003), ensemble-based methods such as the ensemble Kalman filter (Hamill and Snyder, 2002) and the ensemble transform Kalman filter (Bishop et al., 2001). Many research findings on targeted observations have been applied in field experiments, confirming their effectiveness in improving forecast skills (Qin et al., 2022; Szunyogh et al., 2000).

Research on the sensitive area of IOD targeted observation is limited. Feng et al. (2017) used ensemble methods to explore observing locations (i.e., sensitive areas) in the tropical Indian Ocean for advancing beyond the WPB phenomenon of IOD events. They suggested that by increasing observations in the sensitive area and improving initial field accuracy, it can reduce prediction errors in winter, weaken or even eliminate the WPB phenomenon, and finally improve the forecast skill of IOD events. In this study, we will continue to focus on the impact of initial sea temperature errors in the tropical Indian Ocean on IOD predictions, with a focus on the SPB phenomenon. After exploring observing locations (i.e., sensitive areas) for advancing beyond the SPB, we further comparing their respective impacts on the IOD predictability with the sensitive areas associated with the WPB phenomenon in Feng et al. (2017).

The subsequent sections of the paper are structured as follows: Section 2 details the model and experimental strategy. Section 3 delves into the impact of initial error patterns on prediction uncertainties in summer. Section 4 investigates the sensitive areas for advancing beyond the SPB of IOD events. Finally, Section 5 concludes with a summary and discussion.

2. Model and experimental strategy

2.1. Model

The geophysical fluid dynamics laboratory climate model version 2p1 (GFDL CM2p1) is used in this study, which includes ocean,

atmosphere, land, and sea ice components. The ocean component is the Modular Ocean Model version 4 (MOM4p1; Griffies, 2009) released in December 2009, replacing the MOM4.0 used in the CM2.1 version. The equations and methods of MOM4p1 are based on the hydrostatic and nonBoussinesq equations of the ocean along with a selection of subgrid scale (SGS) parameterizations. The ocean component is a numerical representation of the ocean's hydrostatic primitive equations. The horizontal resolution is $1^\circ \times 1^\circ$ in most areas, and the meridional resolution is $1/3^\circ$ in the equatorial region. Totally, there are 50 vertical layers, with a resolution of 10 m in the upper 225 m. The atmosphere component, AM2p12b (GFDL Global Atmospheric Model Development Team, 2004), has a horizontal resolution of 2° (latitude) $\times$ 2.5° (longitude) and 24 vertical layers. It employs a K-profile planetary boundary layer scheme, relaxed Arakawa-Schubert convection, and a parameterization of the vertical momentum transport by cumulus convection. The ocean and atmosphere components are coupled with the Land Dynamics model version 2.1 (LM2.1; Milly and Shmakin, 2002) and the GFDL Sea Ice Simulator (SIS; Delworth et al., 2006). The components of the coupled model exchange fluxes every two hours through the Flexible Modeling System (FMS, http://www.gfdl.noaa.gov/fms) and fluxes are conserved within machine precision.

Feng et al. (2014a) compared the simulation capabilities of 14 coupled models within the Coupled Model Intercomparison Project Phase 5 (CMIP5) with observational data. They found that only four models, including the GFDL CM2p1 coupled model, could capture the climatological conditions and fundamental characteristics of IOD events. Therefore, the GFDL CM2p1 coupled model can be a platform for studying the IOD and its related predictability. For more detailed information about the model, please refer to articles, such as Delworth et al. (2006), Stouffer et al. (2006), and Wittenberg et al. (2006).

2.2. Experimental strategy

We used the forcing (aerosols, land cover, ozone, solar radiation, and radiative gases, etc.) in 1990 to run the model. The initial conditions for the ocean, atmosphere, land and sea ice are consistent with those established by Delworth et al. (2006). The model is run without flux adjustment for 150 years and produces a realistic simulation of the global climate. After a 50 year spin-up period, only the last 100 years are analyzed to reduce the influence of the initial adjustment process. According to the definition of a positive IOD event, 10 positive IOD events are randomly selected as the "true state" (i.e., reference states) (Fig. 1) to be predicted. Most positive IOD events reverse their dipole model index (DMI) signs in the preceding winter, peak in September and October, and reverse the signs again in the following winter, which is consistent with observational conclusions (Wajsowicz, 2004), indicating that the model has captured the characteristics of seasonal phase locking for positive IOD events.

Perfect model predictability experiments are conducted in this study, in which the model is assumed to be perfect, and prediction errors are only caused by initial errors. As the ocean actively forces the atmosphere in the tropical Indian Ocean, only the sea temperature of the ocean component is perturbed. However, initial errors are not superimposed onto all levels of sea temperature, as such perturbations could lead to the incompatibility between the initial fields and the model. This incompatibility may result in significant initial shock, which may conceal the impact of initial errors on the prediction uncertainties of IOD events, particularly in the first few months. As the average thermocline depth in the equatorial Indian Ocean in the GFDL CM2p1 model is 110–130 m (Song et al., 2007), sea temperature anomalies at 95-m depth can to some extent reflect variation in the thermocline depth; additionally, SST is an important variable closely related to the ocean and atmosphere. It is inferred that superimposing initial sea temperature errors on these two layers of ocean can effectively reflect the impact of initial sea temperature errors on the IOD predictability. Therefore, for convenience, we only superimposed initial errors on the sea surface temperature and 95-meter depth temperature fields in the reference state IOD events, and analyzed the impact of initial sea temperature errors on prediction uncertainties of IOD events. Due to the small perturbations in sea temperatures, no significant initial shock occurs during the integrations, even with the use of rigid boundaries.

Considering that the dominant period of IOD events in the model is 4 years (Feng and Duan, 2014), there is usually one positive and one negative IOD event within 4 years. Consequently, the patterns of sea temperature anomalies within 4-year period are plentiful. We selected a set of SSTAs and 95-meter depth temperature anomalies every other month within 4 years preceding each reference state IOD event to make the initial error patterns as plentiful as possible. After scaling each set of temperature anomalies to the same magnitude, we obtained 24 pairs of initial errors for each positive IOD event. By superimposing these initial errors onto the initial temperature fields of reference state IOD events, we integrated the model from six different months: July (-1), October (-1), January (0), April (0), July (0), and October (0) ("-1" represents the year preceding the IOD event, "0" represents the IOD year). Taking July (-1)

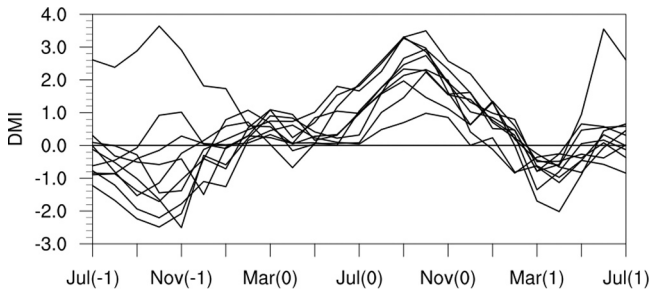

Fig. 1. Evolution of DMI for 10 reference state IOD events ("-1" indicates the year preceding the IOD year; "0" represents the IOD year; "1" denotes the year after the IOD year).

as an example, for each positive IOD event, we superimposed each pair of initial errors onto the initial fields of sea surface temperature and 95-meter depth temperature on July 1st of the year preceding the IOD event. These updated temperature fields are taken as the initial temperature fields on July 1st, while the other initial conditions on July 1st remain unchanged. The model was then integrated starting from July 1st, based on the initial conditions described above. To analyze the development of prediction errors during the summer of IOD years, the model is integrated for 15 months starting from July (-1), and for 12 months starting from other months, respectively. Thus, for each start month, we totally conducted 240 predictions (10 IOD events multiplied by 24 initial errors). To compare with previous work in Feng et al. (2017), we only present the results for start months 7 (-1) and 7 (0) in this paper; results for other start months are similar.

To impartially compare the impact of different initial sea temperature errors on prediction uncertainties of positive IOD events, each pair of initial errors are scaled to the same magnitude as follows. The initial SSTAs and 95-meter depth temperature anomalies are denoted as Q_1 and Q_2, respectively. $Q_{1ij}$and Q_{2ij}represent the values of $Q_1$and Q_2at grid points (i, j) in the Indian Ocean region over 45°E-115°E, 10°S-10°N. Q_1 and $Q_2$are scaled to the same magnitude by$Q'_1 = Q_1/\delta_1$and $Q'_2 = Q_2/\delta_2$, where δ_1 and δ_2 are positive values to make sure the same magnitude between Q_1 and Q_2, and Q'_1 and Q'_2 represent the final initial errors superimposed on the reference state IOD event. The magnitudes of initial errors are represented by $\|Q'_1\| = \sqrt{\sum_{i,j}(Q'_{1ij})^2}$and $\|Q'_2\| = \sqrt{\sum_{i,j}(Q'_{2ij})^2}$, set as 2.4°C in this study. Therefore, the initial errors in the tropical Indian Ocean are smaller than the standard deviation of analysis errors of SSTAs (i.e., 0.2 °C; Kaplan et al., 1998), which indicates that the initial errors in our study may appear in the analysis errors, and the set of initial error magnitude is reasonable.

By superimposing 24 pairs of initial errors on the reference state of each positive IOD event and integrating the model from different start months, 24 predictions are obtained for each positive IOD event from one start month. The prediction errors are defined as the absolute values of the difference in the DMI between the predicted IOD event and the corresponding reference state IOD event. DMI represents the difference in SSTAs between the western pole (50°E-70°E, 10°S-10°N) and the eastern pole (90°E-110°E, 10°S-0°). The time series of DMI have been normalized by their standard deviations. Each year is divided into four seasons, with January-March as the boreal winter, April-June as the boreal spring, and so on. The growth rate κ of prediction errors in each month is calculated by $\kappa = \frac{P_2 - P_1}{\Delta t}$ (1) where P_1 and P_2 represents the prediction errors at time t_1 and t_2, and $\Delta t = t_2 - t_1$, which is set as one month. The growth rate κ of prediction errors in each season is computed as the sum of κ during one season; a positive κ indicates an increase in prediction errors during a season, and a negative value indicates a decrease in prediction errors. A larger positive value of κ indicates a

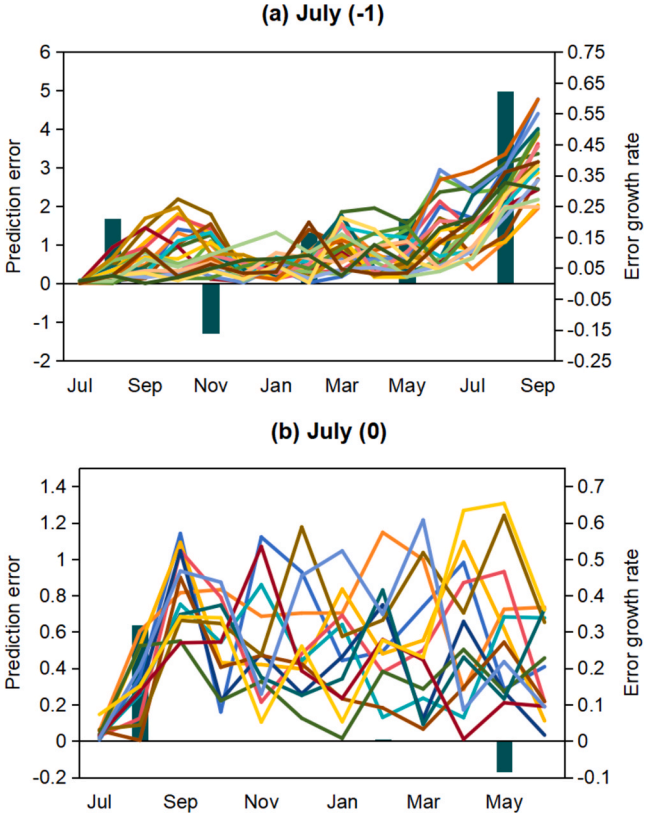

Fig. 2. Time-dependent evolution of prediction errors caused by initial errors that are most likely to cause a significant SPB phenomenon (colored curves) and the ensemble mean of seasonal growth rate (histograms) of the SPB related initial errors for (a) start month July (-1), and (b) start month July (0). Each color line denotes an individual prediction.

faster growth of prediction errors. For each pair of initial errors superimposed on the initial state of positive IOD event, the values of κ are obtained for the four seasons, with the maximum positive slope denoted as κ_{max}, and the second largest positive slope denoted as $\kappa_{s-\ max}$. If $\kappa_{max} > 0.375$ (the top 10 % in slope ranking), and $\kappa_{max} - \kappa_{s-\ max} > 0.06$, we consider the development of prediction errors in the season corresponding to κ_{max} as significant compared to other seasons. A SPB phenomenon refers to the prediction errors with the fastest growth rate κ_{max} in summer. Initial errors satisfying the above criteria with κ_{max} corresponding to the summer season are selected (i.e., SPB-related initial errors), and their dominant characteristics are further analyzed.

3. Effect of initial error patterns on the prediction uncertainties in summer

According to the criteria in Section 2, initial errors that are most likely to cause a significant SPB phenomenon are selected. Fig. 2 shows the evolution of prediction errors caused by these initial errors for different start months. Notably, the prediction errors grow more rapidly in summer compared to other seasons, resulting in large prediction errors in summer, thereby significantly limiting the forecast skill of IOD events. Fig. 3 illustrates the evolution of SSTAs and sea surface wind anomalies over the tropical Indian Ocean for an IOD event starting from July (-1), with and without SPB-related initial errors superimposed. Fig. 3a indicates that a positive IOD event occurs in the tropical Indian Ocean, characterized by a significant west-east dipole pattern in September (0), accompanied by southeasterly wind anomalies at the eastern pole. When SPB-related initial errors are superimposed on the positive IOD event, negative SSTAs emerge in the western Indian Ocean during the mature phase of IOD. As a result, the dipole pattern during the mature phase of IOD event is destroyed, and the magnitude of the DMI significantly decreases. Consequently, these SPB-related initial errors induced large prediction errors, especially in summer, leading to a significant SPB phenomenon. Fig. 3c shows the differences between the patterns with and without the initial errors superimposed, depicting the evolution of these errors. Apparently, a significant west-east dipole pattern occurs in the tropical Indian Ocean from May (0) to September (0), characterized by negative values in the western Indian Ocean and positive values in the eastern Indian Ocean, along with northwest wind anomalies at the eastern pole, which resemble the development of negative IOD events. This evolution of SPB-related initial errors causes large prediction errors in summer

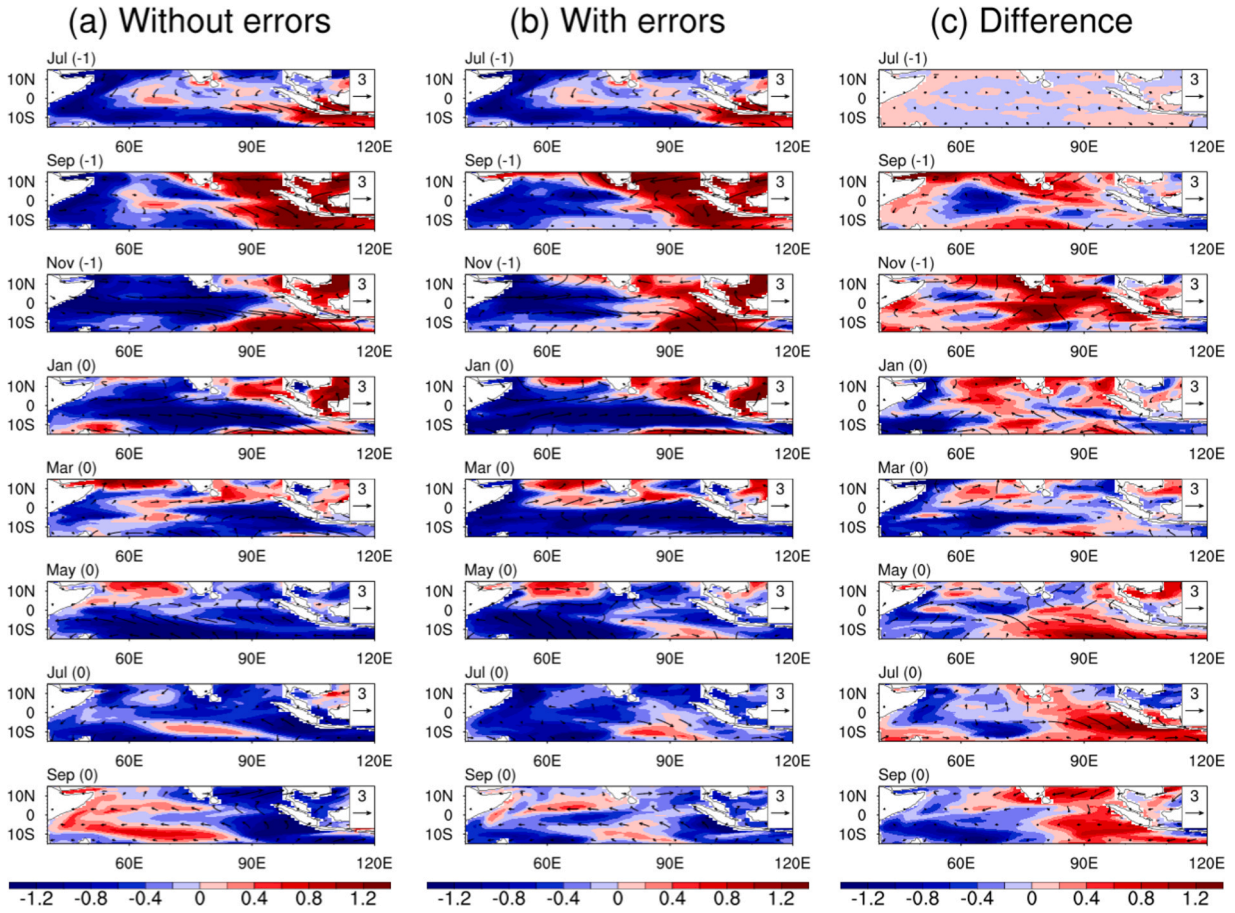

Fig. 3. Evolutions of SSTAs (units: °C) and sea surface wind anomalies (units: m s^{-1}) over the tropical Indian Ocean for an IOD event starting from July (-1), (a) without initial errors superimposed, (b) with SPB-related initial errors superimposed, and (c) the difference in patterns between (b) and (a).

by inducing patterns that oppose the reference state IOD event.

To delve deeper into the SPB phenomenon, a Combined Empirical Orthogonal Function (CEOF) analysis is conducted for each start month on both the surface and subsurface components of the initial errors that are most likely to cause a significant SPB phenomenon. The spatial distributions of CEOF1 for different start months are illustrated in Fig. 4, with explanatory variances of 32.3 % for the start month July (-1) and 31.2 % for the start month July (0), respectively. The surface and subsurface components of CEOF1 prominently present an east-west dipole mode, with the subsurface temperature anomalies exhibiting greater magnitude than the surface temperature anomalies. Notably, the subsurface component of CEOF1 is similar to the temperature anomaly pattern observed during the mature phase of a positive IOD event, characterized by large value centers in the southern sector of the western pole and the equatorial eastern Indian Ocean. Meanwhile, the surface component of CEOF1 exhibits various spatial patterns for different start months. In the case of the start month July (-1), the large value area is located in the southeastern Indian Ocean, where SSTAs typically first emerge and intensify during the development of IOD events. For the start month July (0), the large value area extends across the central southern Indian Ocean, where the Ekman ridge is located and is closely related to the development of SSTAs in the western pole of IOD. These initial errors exhibit spatial patterns resembling those most likely to cause a significant WPB as documented by Feng et al. (2017). It is important to note that, in addition to the spatial patterns of initial errors, the occurrence of predictability barriers is also closely related to other factors, such as IOD events themselves, climate state, and influences from the Pacific Ocean (Feng et al., 2014b; Liu et al., 2018). In this study, we focus exclusively on the initial errors that lead to a significant SPB.

Are initial errors with an east-west dipole pattern more likely to cause a significant SPB than those with other spatial patterns? To address this issue, we superimposed initial errors with a dipole pattern and spatially correlated noises on the initial fields of reference state IOD events. Subsequently, we analyzed the development of these initial errors to understand their impact on prediction uncertainties. Specifically, we select 10 sets of initial errors that are most likely to cause a significant SPB from the 240 sets of initial errors for each start month. These initial errors have the highest absolute correlation coefficients with the leading mode of the corresponding CEOF (i.e., CEOF1), suggesting a close resemblance to the spatial pattern of CEOF1. Consequently, these initial errors are identified as the dipole pattern initial errors. In comparison, three sets of spatially correlated noises with equal magnitude as the dipole pattern initial errors are generated following the method outlined in Feng et al. (2017). The spatial patterns of these spatially correlated noises are shown in Fig. 5, which are totally different from the dipole pattern initial errors. Then we superimpose three sets of spatially correlated noises on the initial fields of 10 reference state IOD events. After 15 months of integration for the start month July (-1) and 12 months for the start month July (0), respectively, a total of 30 predictions are generated for each start month. The evolution of prediction errors after superimposing these initial errors with various spatial patterns onto the reference state IOD events are analyzed.

The analysis in Fig. 6 focuses on the prediction errors in summer caused by dipole pattern initial errors and three sets of spatially correlated noises for each start month. It is evident that, in most cases, the prediction errors in summer caused by dipole pattern initial errors are larger than those caused by spatially correlated noises for all the start months, which is especially evident in their composite. This underscores the significant impact of initial errors with a dipole pattern on the prediction uncertainties in summer compared to the spatially correlated noises. Additionally, the seasonal growth rates of prediction errors caused by these dipole pattern initial errors and spatially correlated noises for each start month (as shown in Table 1) are further analyzed. The table illustrates that, irrespective of the start month, the seasonal growth rates of prediction errors caused by dipole pattern initial errors display distinct seasonality, with fastest error growth occurring during summer, indicating the presence of the SPB phenomena. In contrast, the seasonal growth rates of prediction errors caused by the spatially correlated noises do not exhibit the seasonality as distinct as the dipole pattern initial errors, especially for the start month July (-1). Although the prediction errors caused by some spatially correlated noises have the largest

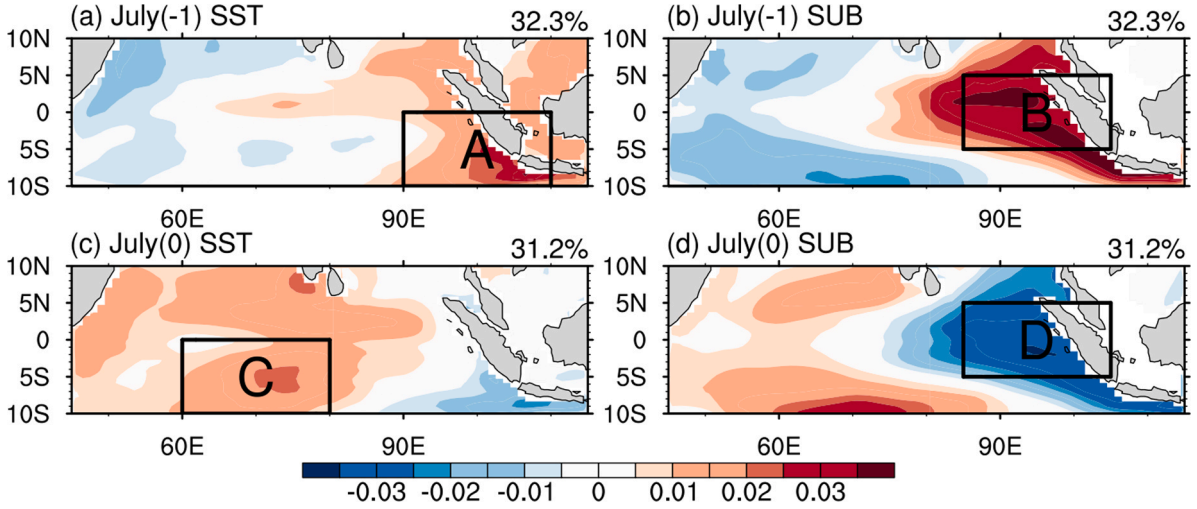

Fig. 4. The surface (a) and subsurface (b) temperature errors of CEOF1 for initial errors that are most likely to cause a significant SPB phenomenon for start month July (-1); (c) and (d) are as above, but for start month July (0); the black boxes labeled A, B, C, and D represent the regions where the large values of CEOF1 are located (units: °C).

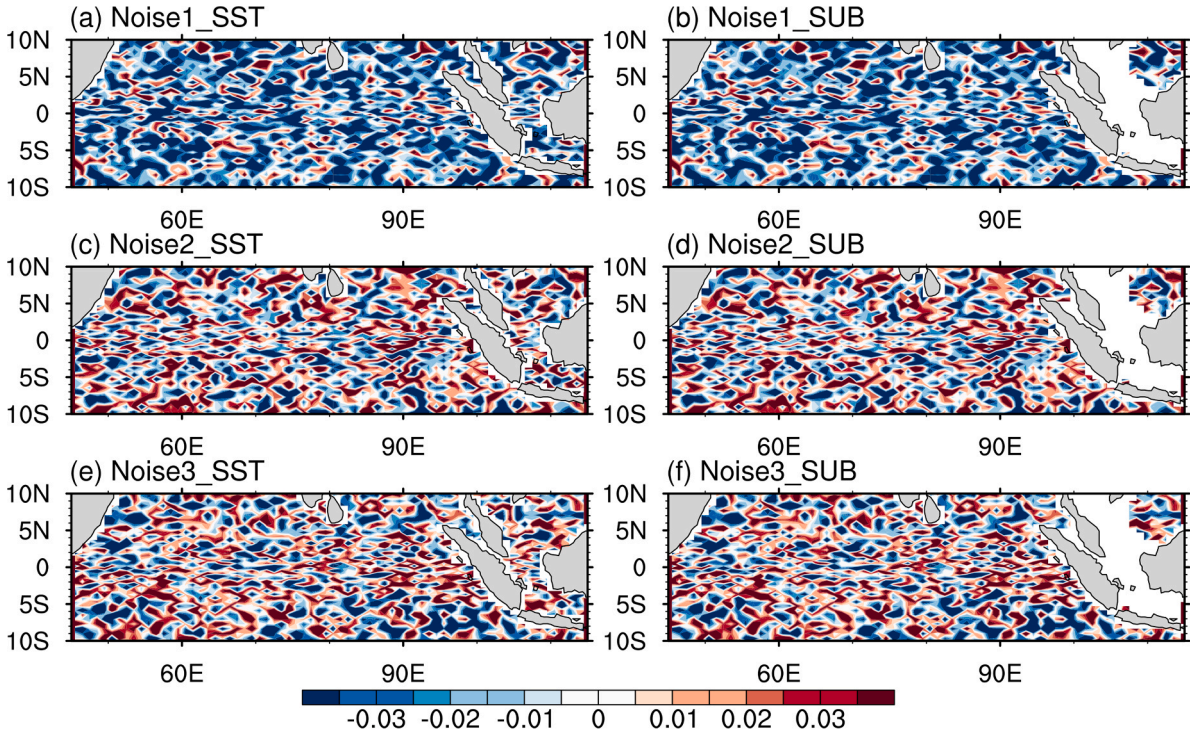

Fig. 5. The surface (a, c, e) and subsurface (b, d, f) components of three sets of spatially correlated noises (units: °C).

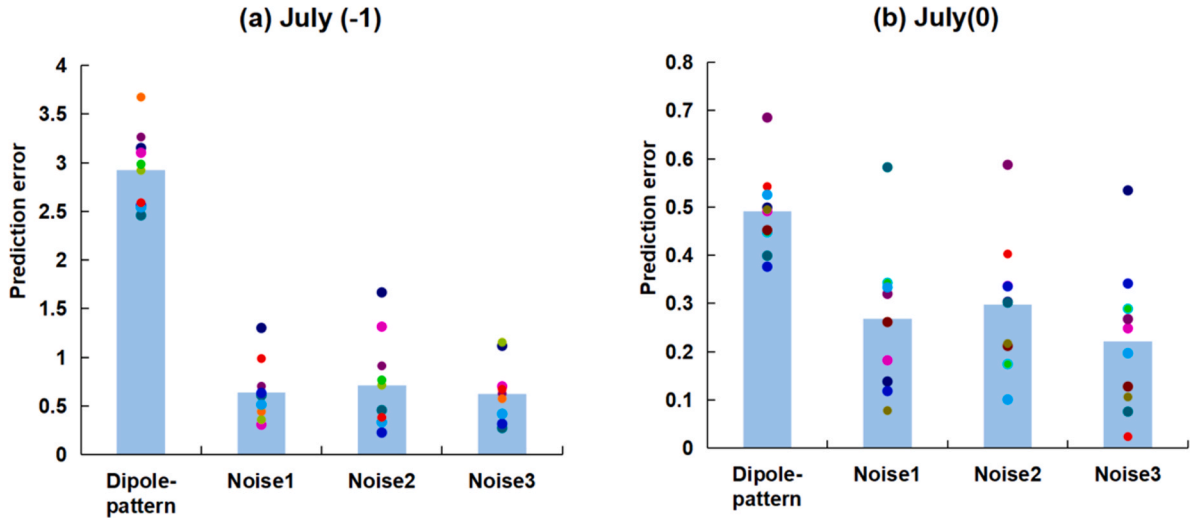

Fig. 6. The prediction errors in summer that caused by dipole pattern initial errors and three sets of spatially correlated noises for (a) the start month July (−1), and (b) the start month July (0) (color plots). The bars illustrate the average prediction errors for each type of initial errors in summer.

growth rates in summer, the growth rates in summer is not as large as those caused by the dipole pattern initial errors. That is, the prediction errors caused by the dipole pattern initial errors exhibit notably faster growth in summer compared to other seasons, leading to a significant SPB phenomenon. Conversely, spatially correlated noises may induce a weaker SPB phenomenon or potentially no SPB phenomenon at all.

These findings highlight that initial errors characterized by a dipole pattern mode result in larger prediction errors in summer compared to spatially correlated noises. Moreover, these dipole pattern initial errors cause the most rapid growth of prediction errors in summer compared to other seasons, ultimately resulting in the occurrence of a significant SPB phenomenon. The occurrence of the significant SPB is closed linked to the specific spatial structure of initial sea temperature errors in the tropical Indian Ocean. By

Table 1
The composite seasonal growth rates of prediction errors caused by dipole pattern initial errors and three sets of spatially correlated noises for start months July (−1) and July (0).

From July (-1)				
Composite$_K$	**OND**	**JFM**	**AMJ**	**JAS**
Dipole pattern errors	−0.227	0.240	0.260	**0.878**
Correlated noise 1	0.124	−0.148	0.353	**0.164**
Correlated noise 2	0.110	0.046	0.280	**0.242**
Correlated noise 3	0.063	−0.071	0.202	**0.122**
From July (0)				
Composite$_K$	**JAS**	**OND**	**JFM**	**AMJ**
Dipole pattern errors	**0.481**	−0.001	0.005	−0.231
Correlated noise 1	**0.216**	0.017	−0.019	0.063
Correlated noise 2	**0.254**	−0.114	0.166	−0.031
Correlated noise 3	**0.195**	0.047	0.181	0.087

effectively filtering out these dipole pattern initial errors through intensive observations, we can probably reduce prediction errors in summer and potentially mitigating or even eliminating the SPB phenomenon, ultimately improving the forecast skill for positive IOD events. However, carrying out intensive observations in the vast Indian Ocean comes with a substantial economic cost. Therefore, targeted observation strategy is probably a useful approach as stated in the introduction, in which the sensitive areas for additional observations need to be identified. As previously noted, the large values of these dipole pattern initial errors are localized within a few areas and exhibit local characteristics, implying that the initial errors in these regions contribute significantly to prediction uncertainties. These areas may represent sensitive areas for targeted observations in positive IOD predictions, which will be further identified in the following analysis.

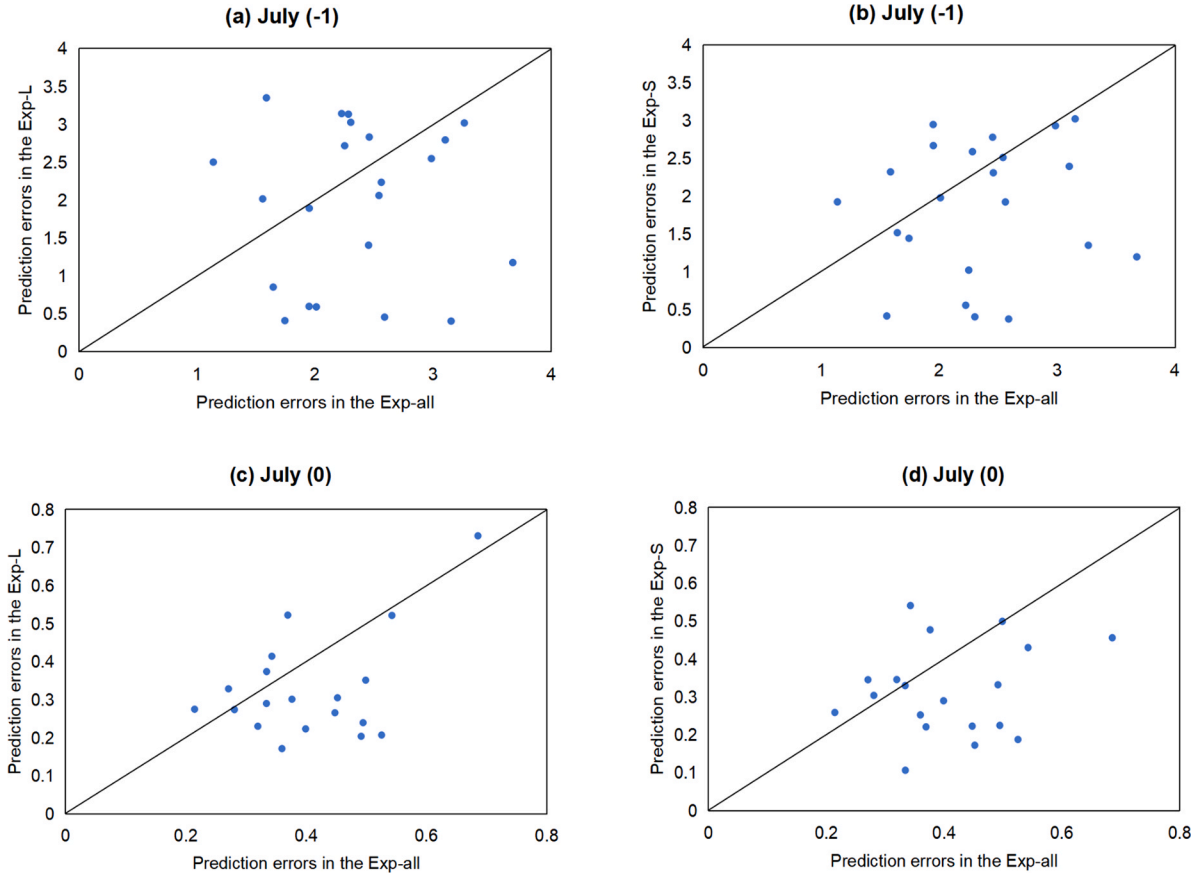

Fig. 7. The prediction errors in summer for each case in different experiments; the y-axis represents the prediction errors in Exp-L (a and c), and in Exp-S (b and d); while the x-axis shows those in Exp-all. Graphs a and b illustrate the results for the start month July (−1), whereas graphs c and d correspond to the start month July (0).

4. Identification of sensitive areas in the tropical Indian ocean for advancing beyond the SPB

In this section, by conducting sensitivity experiments, we identified the sensitive areas of targeted observations for positive IOD events. For the start month July (-1), the large values of dipole pattern initial errors are mainly located at 10°S-0°, 90°E-110°E (i.e., A of Fig. 4a) in the surface component, and at 5°S-5°N, 85°E-105°E (i.e., B of Fig. 4b) in the subsurface component. For the start month July (0), the large values of dipole pattern initial errors are mainly located at 10°S-0°, 60°E-80°E (i.e., C of Fig. 4c) in the surface component, and at 5°S-5°N, 85°E-105°E (i.e., D of Fig. 4d) in the subsurface component. A, B, C, and D are of the same size. The initial errors that are most likely to cause a significant SPB phenomenon are chosen to conduct the sensitivity experiments, and labeled as "the whole initial errors". The corresponding predictions, with these whole initial errors superimposed, cause significant SPB phenomena and are denoted as Exp-all. For the start month July (-1), for each pair of whole initial errors, we simultaneously eliminate the initial errors at A from the surface component and at B from the subsurface component. Then the remaining initial errors are superimposed on the same initial fields as the whole initial errors in Exp-all and the model is run for 15 months. Similarly, for the start month July (0), initial errors at C from the surface component and at D from the subsurface component are eliminated. Subsequently, the remaining initial errors are superimposed on the respective initial fields and the model is integrated for 12 months. This set of experiments is referred to as Exp-S. In contrast, for the start month July (-1) (July (0)), we only superimpose the initial errors within the large value areas A (C) and B (D) to the same initial fields as the whole initial errors, and the rest of the whole initial errors are eliminated. Then we integrate the model for 15 (12) months and obtain the predictions. This set of experiments is called Exp-L. The only difference among these three types of experiments lies in the different initial errors superimposed on the initial fields.

An analysis of prediction errors in summer in Exp-all, Exp-S, and Exp-L is shown in Fig. 7. The points located beneath the diagonal line suggest that the prediction errors in summer in Exp-all are larger than those in Exp-S and Exp-L. Notably, the majority of points are located beneath the diagonal line in both start months, signifying that for most cases, prediction errors in summer in Exp-all are larger than those in Exp-S or Exp-L. Consequently, partially eliminating initial errors from the whole initial errors (i.e., the Exp-S or the Exp-L) significantly reduces prediction errors in summer, thereby improving the forecast skill of positive IOD events spanning summer. It is noted that, in some cases, Exp-S or Exp-L cause larger prediction errors than Exp-all. This can be attributed to the opposite effects of initial errors within large value areas and those outside these areas on the signs of prediction errors. Initial errors outside the large value areas may partially cancel the effects of initial errors within these areas on predictions by some amount. In this condition, keeping the full initial errors probably reduces predictions errors. Similar phenomena are also observed in Yu et al. (2012), which

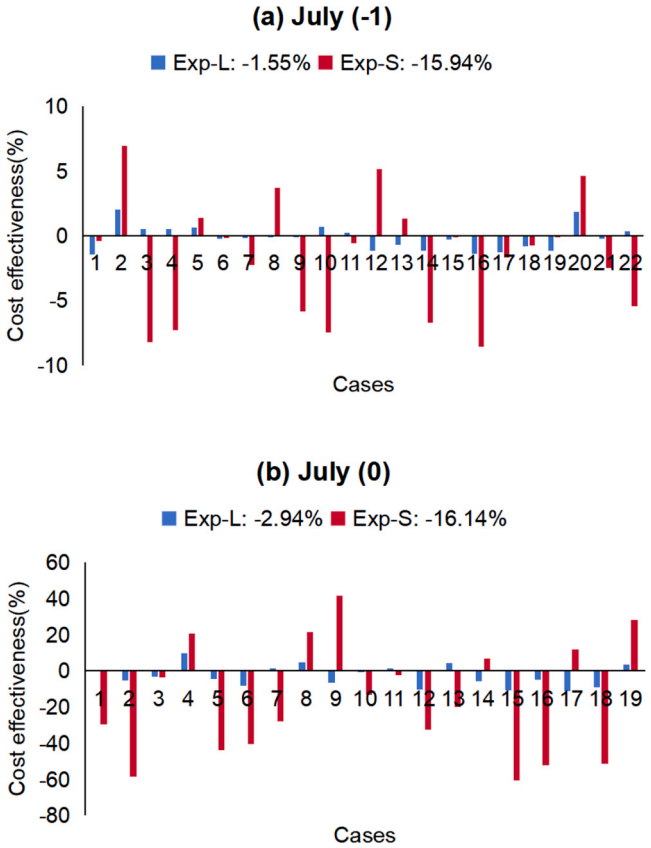

Fig. 8. The cost effectiveness of eliminating initial errors within one unit area for each individual case in Exp-S and Exp-L for (a) the start month July (−1); and (b) the start month July (0); the numbers above the graphs are the average cost effectiveness in different experiments.

identified the sensitive areas of ENSO using the Zebiak-Cane model. Of course, this is just one possible explanation for the occurrence of worse forecast skill, it might also be due to the imbalance among different variables after elimination of initial errors in Exp-S and Exp-L.

Given that the area from which the initial errors in Exp-S are eliminated, is merely one-sixth of that in Exp-L, to impartially compare the effects of eliminating initial errors within one unit area in different experiments on prediction uncertainties, we defined the cost effectiveness C as $C = \mathrm{Im}pact/N = ((E_1 - E_0)/E_0)/N$, where *Impact* denotes the effect of eliminating initial errors in different experiments on prediction errors in summer compared to Exp-all, E_0 and E_1 signify the prediction errors in summer in Exp-all and Exp-S (or Exp-L), and N denotes the area size from which initial errors are eliminated. N is set as 6 in Exp-L and 1 in Exp-S, for simplicity. A negative or positive value of C indicates a reduction or increase in prediction errors during summer, leading to an improvement or decline in forecast skill spanning summer by eliminating the initial errors per unit area. A larger absolute value of negative C signifies a greater improvement in forecast skill. Fig. 8 illustrates the effects of eliminating initial errors per unit area in different experiments for different start months. The results reveal that, for most cases, C is negative in both Exp-S and Exp-L, indicating that eliminating initial errors per unit area in these experiments can effectively decrease prediction errors in summer and improve the forecast skills of IOD events spanning summer. On average, the absolute value of C is higher in Exp-S than in Exp-L, demonstrating that eliminating initial errors within one unit area in Exp-S leads to a greater reduction in prediction errors and greater improvement of the forecast skills compared to Exp-L. This is further illustrated by their average values: the average cost effectiveness is −15.94 % and −16.14 % in Exp-S, while it is −1.55 % and −2.94 % in Exp-L, for two start months, respectively. This indicates that by solely eliminating initial errors in one-seventh of the tropical Indian Ocean in Exp-S, the prediction errors in summer can be significantly reduced by approximately 16 %, whereas in Exp-L, the reduction is only about 2 %. As previous mentioned, the large value areas (i.e., A, B, C, and D) are closely associated with the development of IOD events, initial errors in these areas (i.e., Exp-L) probably develop rapidly under the Bjerknes feedback, resulting in large prediction errors. Conversely, when eliminating initial errors in these large value areas (i.e., Exp-S), the prediction errors are largely reduced.

The evolution of SSTAs over the tropical Indian Ocean for an IOD event starting from July (-1) in different experiments are presented in Fig. 9. Fig. 9a depicts the SSTA evolution of the reference positive IOD event. However, the positive IOD event is predicted as a negative IOD event in Exp-all, resulting in large prediction errors in summer and indicating the occurrence of SPB. Although Exp-L exhibits reduced prediction errors in summer compared to Exp-all, it still fails to accurately predict the positive IOD event. Conversely, Exp-S shows the development of a positive IOD event that closely resembles the reference IOD, resulting in smaller prediction errors in summer. In summary, the prediction errors in summer in Exp-S and Exp-L are smaller than those in Exp-all, especially in the case of Exp-S. This indicates that the prediction uncertainties in summer are particularly sensitive to initial errors at A and B (C and D) for start month July (-1) (July (0)).

As illustrated in Fig. 4, it is evident that initial errors in the subsurface large value areas of CEOF1 are greater than those in the surface large value areas. Prediction uncertainties in summer are particularly sensitive to initial errors within these large value areas. This raises the question of whether prediction errors in summer are more sensitive to initial errors in the subsurface large value areas

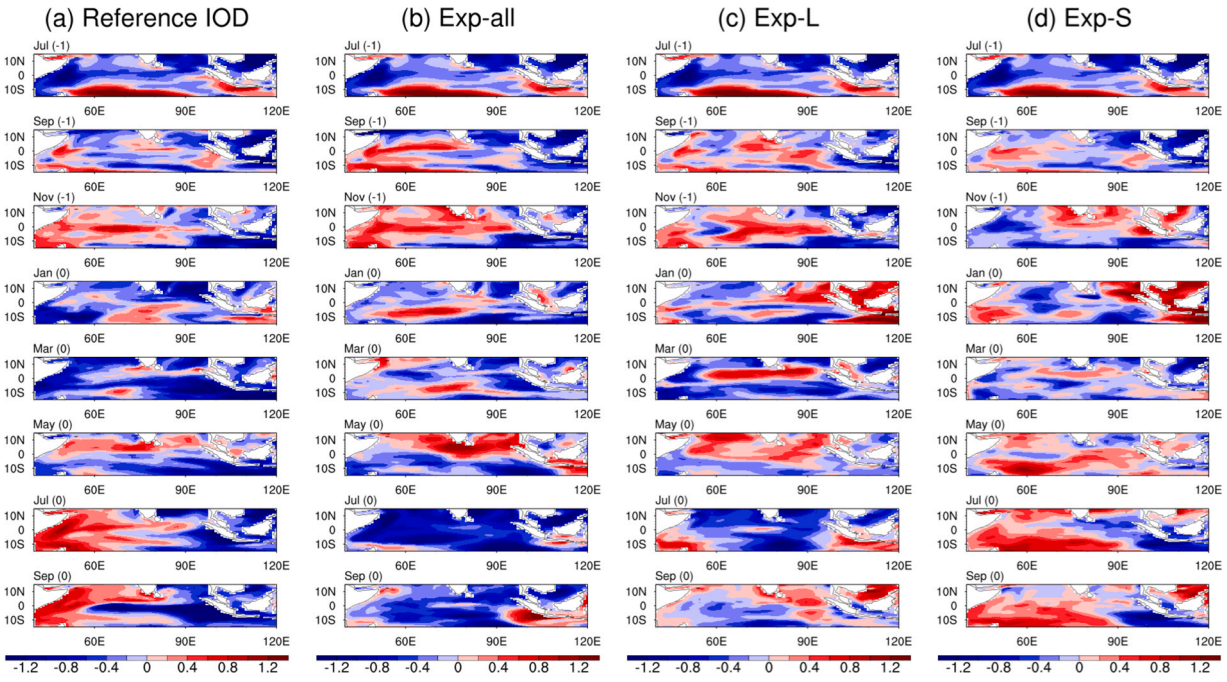

Fig. 9. Evolutions of SSTAs (units: °C) over the tropical Indian Ocean for an IOD event starting from July (-1) for (a) the reference state IOD event, (b) Exp-all, (c) Exp-L, and (d) Exp-S.

compared to those in the surface large value areas. To investigate this further, we conducted another sets of experiments. For the start month July (-1), we eliminated initial errors within surface large value area A and subsurface large value area B from the whole initial errors, respectively. For the start month July (0), we eliminated initial errors within large value areas C and D from the whole initial errors, respectively. The remaining initial errors were then superimposed on the same initial fields as the whole initial errors in Exp-all and integrated for 15 or 12 months for different start months. The experiments that eliminating initial errors in the surface large value areas were denoted as Exp-surf, while those targeting the subsurface large value areas were labeled as Exp-sub. As the sizes of the areas from which the initial errors are eliminated in Exp-surf and Exp-sub are the same, we merely compare the impact of eliminating initial errors on the prediction uncertainties in summer, defined as $\mathrm{Im}pact = (E_1 - E_0)/E_0$, where E_0 and E_1 signify the prediction errors in summer in Exp-all and Exp-surf (or Exp-sub). Negative *Impact* indicates a decrease in prediction errors during summer compared to the Exp-all, while positive *Impact* indicate an increase. In Fig. 10, most cases show negative values of *Impact* in Exp-surf and Exp-sub for both start months, indicating that by merely eliminating the initial errors in either the surface or subsurface large value area significantly reduces prediction errors in summer when compared to Exp-all. Notably, eliminating solely the initial errors in the subsurface large value area results in higher absolute values of *Impact* than those regarding the surface large value areas for both start months. Specifically, the composite values are −19.60 % (-17.22 %) in Exp-sub and −13.78 % (-11.57 %) in Exp-surf for the start month July (-1) (July (0)). It is worth noting that, the area where initial errors are eliminated in Exp-sub is only half the size of that in Exp-S. Despite this, the improvements in Exp-sub are larger than those in Exp-S. That is, by solely eliminating initial errors in one fourteenth of the tropical Indian Ocean in Exp-sub, the prediction errors in summer can be significantly reduced by more than 17 %. This suggests that solely eliminating initial errors in the subsurface large value area can largely decrease prediction errors in summer, and greatly improve the forecast skill. Thus, the prediction errors in summer are more sensitive to initial errors in the subsurface large value areas, and this area (i.e., 5°S-5°N, 85°E-105°E, at 95-meter depth) is the sensitive area of targeted observations for advancing beyond the SPB for positive IOD events. These results underscore the importance of conducting intensive observations in the subsurface large value area. By assimilating additional observations in this area to improve the accuracy of initial fields, prediction errors in summer are largely reduced, leading to an improvement in the IOD forecast skill. Specifically, the sensitive areas for advancing beyond the SPB and the WPB coincide within the same region (Feng et al., 2017). Thus, conducting intensive observations in this area not only reduce prediction errors in summer but also in winter, ultimately improving the forecast skill of IOD events.

As illustrated above, sensitive areas of targeted observations for advancing beyond the WPB and SPB for positive IOD events are located within a specific area (specifically, 5°S-5°N, 85°E-105°E, at a depth of 95 m) in the tropical Indian Ocean. Notably, prediction errors in both summer and winter are sensitive to initial errors within this area. Consequently, if intensive observations are conducted

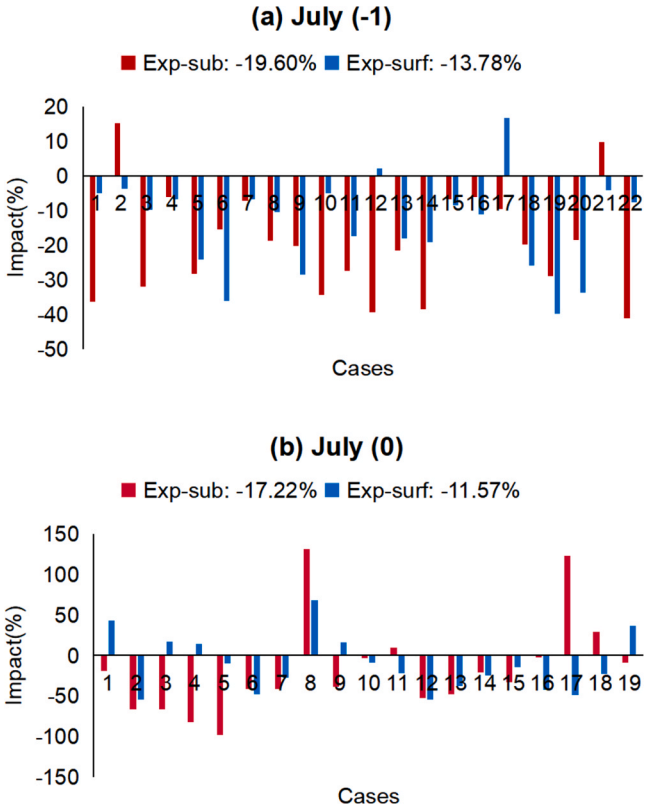

Fig. 10. The impacts of eliminating initial errors for each individual case on the prediction errors in summer in Exp-surf and Exp-sub for (a) the start month July (-1); and (b) the start month July (0); the numbers above the graphs represent the average impacts in different experiments.

in this area, which season—winter or summer—would show a more significant reduction in prediction errors? To delve deeper into this question, we compared the impacts of eliminating initial errors in the sensitive area (i.e., Exp-sub) on prediction errors in summer and winter. The impacts in winter are referred to the results in Feng et al. (2017). The impacts is −50.14 % (-59.96 %) in winter and −19.60 % (-17.22 %) in summer for the start month July (-1) (July (0)). Remarkably, for both start months, the absolute values of impacts are larger in winter compared to summer. When initial errors in the sensitive area are eliminated, prediction errors decrease rapidly, with a greater reduction in winter than summer. Therefore, conducting intensive observations in this sensitive area, a more substantial reduction in prediction errors during winter, as opposed to summer, can be achieved, significantly improving the forecast skill of IOD events.

5. Summary and conclusions

This article utilizes the GFDL CM2p1 model to conduct perfect model predictability experiments, identifying the sensitive area of targeted observations in the tropical Indian Ocean for advancing beyond the SPB of positive IOD predictions. In these perfect model predictability experiments, the model is assumed to be perfect, and prediction errors are solely caused by initial errors.

The study initially delves into exploring the impact of initial error patterns on prediction uncertainties by comparing dipole pattern initial errors with three sets of spatially correlated noises. The findings reveal that dipole pattern initial errors, as opposed to spatially correlated noises, result in larger prediction errors in summer, characterized by a pronounced seasonality dependence with the fastest error growth in summer. In contrast, prediction errors stemming from spatially correlated noises demonstrate a lower growth rate in summer, potentially leading to weaker or no SPB.

Furthermore, the large values of these dipole pattern initial errors tend to be concentrated within specific areas. To assess the impact of initial errors within these large value areas on prediction uncertainties in summer, a series of sensitivity experiments were conducted. By partially eliminating initial sea temperature errors in the tropical Indian Ocean (i.e., Exp-S and Exp-L), and superimposing the remaining initial errors on the initial analysis fields of the corresponding IOD events, the prediction errors in summer are largely reduced. Particularly noteworthy was the significant decrease in prediction errors during summer when eliminating initial errors in both the surface and subsurface large value areas simultaneously (i.e., Exp-S), highlighting the sensitivity of prediction uncertainties in summer to initial errors within these specific regions. The outcomes suggest that by eliminating initial sea temperature errors in these large value areas, a notable reduction in prediction errors during summer can be achieved, potentially weakening or even eliminating the SPB phenomenon and improving the forecast skill of IOD events.

We further conducted another set of experiments to explore the impact of initial sea temperature errors in the surface and subsurface large value areas on prediction uncertainties of IOD events in summer. Eliminating initial errors in the surface (i.e., Exp-surf) and subsurface (i.e., Exp-sub) large value areas individually resulted in a decrease in prediction errors during summer, with a more pronounced reduction observed when eliminating initial errors in the subsurface large value area. This highlights the sensitivity of prediction uncertainties in summer to initial errors in the subsurface large value area. Therefore, the subsurface large value area of dipole pattern initial errors can be considered as a sensitive area of targeted observations for positive IOD event prediction. Notably, this sensitive area aligns with the region identified by Feng et al. (2017) for advancing beyond the WPB. Eliminating initial errors in this sensitive area led to a greater reduction in prediction errors during winter compared to summer, regardless of the start months.

Mu et al. (2017) reported that the mechanism of the evolution of the IOD signal could explain the error growth, and that Bjerknes positive feedback is responsible for error growth. Therefore, it is supposed that the reason for the strongest IOD signal occurring in the equatorial subsurface region of the eastern Indian Ocean (i.e., the sensitive area) may also explain why error growth is particularly pronounced in this area. The initial errors located in the equatorial subsurface eastern Indian Ocean acts as a trigger of Bjerknes positive feedback. It will lead to deepening (or shallowing) of the thermocline, which subsequently affects the thermocline–SST feedback. The altered SST further affects the sea surface wind field, inducing downwelling (or upwelling) Kelvin waves that, in turn, deepen (or shallow) the thermocline in the equatorial eastern Indian Ocean. Consequently, the positive (or negative) initial errors within this sensitive area are amplified and error growth is particularly pronounced in this area. Hence, carrying out intensive observations in this specific region and assimilating additional data to improve the accuracy of initial analysis fields can effectively weaken or eliminate the predictability barriers, ultimately improving the forecast skill of IOD events. Luo et al. (2007) pointed out that they failed to predict the strong cold signal in the eastern pole of the 1997 IOD using the Scale Interaction Experiment Frontier (SINTEX-F) model, which is mainly due to initial errors in the subsurface Indian Ocean. Wajsowicz (2005) emphasized that the lack of proper initialization of subsurface ocean observations significantly limits the forecast skill of the eastern pole. These studies have highlighted the importance of increasing observations in the subsurface ocean and improving the accuracy of initial fields, which is consistent with our conclusions.

This study suggests that increasing observations in the sensitive area in the tropical Indian Ocean lead to a greater reduction in prediction errors during winter than summer, leading to a more substantial improvement in forecast skill during the winter season. Previous researches by Liu et al. (2018) and Feng and Duan (2018) have shown that initial sea temperature errors with specific spatial patterns in the tropical Pacific Ocean can lead to a significant SPB phenomenon. This suggests that aside from initial errors in the tropical Indian Ocean, the prediction uncertainties in summer are also sensitive to initial errors in the tropical Pacific Ocean. Sensitive areas in the tropical Pacific Ocean for advancing beyond the SPB phenomenon probably exist. If this sensitive area in the tropical Pacific Ocean for positive IOD event predictions is further identified and then intensive observations are conducted in that area, it may further reduce prediction errors in summer and greatly improve the forecast skill of IOD events. Moreover, we focused solely on the impact of initial sea temperature errors in the tropical Indian Ocean on IOD predictability. Given that the IOD is a coupled ocean-atmosphere event, uncertainties in the initial conditions of other variables also play a significant role in IOD predictability.

Hence, in our forthcoming research endeavors, we aim to delve deeper into the effects of coupled initial errors on IOD predictability.

CRediT authorship contribution statement

Duan Wansuo: Writing – review & editing, Supervision, Project administration, Methodology, Funding acquisition, Conceptualization. **Feng Rong:** Writing – review & editing, Writing – original draft, Visualization, Software, Investigation, Formal analysis, Conceptualization, Funding acquisition.

Declaration of Competing Interest

The authors declare that they have no known competing financial interests or personal relationships that could have appeared to influence the work reported in this paper.

Acknowledgements

The study is supported by the National Natural Science Foundation of China (Grants No. 42330111, 42475060). We would like to thank Shanghai Frontiers Science Center of Atmosphere-Ocean Interanction for their support.

Data availability

Data will be made available on request.

References

Behera, S.K., Luo, J.J., Masson, S., Rao, S.A., Sakuma, H., Yamagata, T., 2006. A CGCM study on the interaction between IOD and ENSO. J. Clim. 19 (9), 1688–1705.
Bishop, C.H., Etherton, B.J., Majumdar, S.J., 2001. Adaptive sampling with the ensemble transform Kalman filter. PartI: Theoretical aspects. Mon. Wea. Rev. 129, 420–436.
Cai, W., Hendon, H.H., Meyers, G., 2005. Indian Ocean dipole variability in the CSIRO Mark 3 coupled climate model. J. Clim. 18, 1449–1468.
Cai, W., Yang, K., Wu, L., Huang, G., Santoso, A., Ng, B., Wang, G., Yamagata, T., 2020. Opposite response of strong and moderate positive Indian Ocean Dipole to global warming. Nat. Clim. Change 11, 27–32. https://doi.org/10.1038/s41558-020-00943-1.
Delworth, T.L., et al., 2006. GFDL's CM2 global coupled climate models. Part I: Formulation and simulation characteristics. J. Clim. 19, 643–674.
Du, Y., Zhang, Y., Zhang, L., Tozuka, T., Ng, B., Cai, W., 2020. Thermocline warming induced extreme Indian Ocean Dipole in 2019. Geophys. Res. Lett. 47 (18). https://doi.org/10.1029/2020GL090079.
Duan, J., Li, Y., Zhang, L., Wang, F., 2020. Impacts of the Indian Ocean Dipole on sea level and gyre circulation of the western tropical Pacific Ocean. J. Clim. 33, 4207–4288.
Feng, M., Meyers, G., 2003. Interannual variability in the tropical Indian Ocean: a two-year time-scale of Indian Ocean Dipole. Deep-Sea Res. II 50, 2263–2284.
Feng, R., Duan, W.S., 2014. The spatial patterns of initial errors related to the "winter predictability barrier'' of the Indian Ocean dipole. Atmos. Ocean. Sci. Lett. 7 (5), 406–410. https://doi.org/10.3878/j.issn.1674-2834.14.0018.
Feng, R., Mu, M., Duan, W.S., 2014a. Study on the "winter persistence barrier'' of Indian Ocean dipole events using observation data and CMIP5 model outputs. Theor. Appl. Climatol. 118 (3), 523–534.
Feng, R., Duan, W.S., Mu, M., 2014b. The "winter predictability barrier" for IOD events and its error growth dynamics: Results from a fully coupled GCM. J. Geophys. Res: Oceans 119. https://doi.org/10.1002/2014JC010473.
Feng, R., Duan, W.S., Mu, M., 2017. Estimating observing locations for advancing beyond the winter predictability barrier of Indian Ocean dipole event predictions. Clim. Dyn. 48, 1173–1185. https://doi.org/10.1007/s00382-016-3134-3.
Feng, R., Duan, W.S., 2019. Indian Ocean Dipole-related predictability barriers induced by initial errors in the tropical Indian Ocean in a CGCM. Adv. Atmos. Sci. 36, 658–668. https://doi.org/10.1007/s00376-019-8224-9.
GFDL Global Atmospheric Model Development Team, 2004. The new GFDL global atmosphere and land model AM2–LM2: Evaluation with prescribed SST simulations. J. Clim. 17, 4641–4673.
Griffies, S.M., 2009. Elements of MOM4p1: GFDL Ocean Group. Technical Report No. 6, NOAA/Geophysical Fluid Dynamics Laboratory, Princeton, N. J.
Guo, F., Liu, Q., Sun, S., Yang, J., 2015. Three types of Indian Ocean Dipoles. J. Clim. 28, 3073–3092.
Hamill, T.M., Snyder, C., 2002. Using improved background-error covariance from an ensemble Kalman filter for adaptiveobservations. Mon. Wea. Rev. 130, 1552–1572.
Huang, P., Zheng, X.T., Ying, J., 2019. Disentangling the changes in the Indian Ocean Dipole-related SST and rainfall variability under global warming in CMIP5 modes. J. Clim. 32 (13), 3803–3818.
Hui, C., Zheng, X.T., 2018. Uncertainty in Indian Ocean Dipole response to global warming: the role of internal variability. Clim. Dyn. 51. https://doi.org/10.1007/s00382-018-4098-2.
Kaplan, A., Cane, M.A., Kushnir, Y., Clement, A.C., Blumenthal, M.B., Rajagopalan, B., 1998. Analyses of global sea surface temperature 1856–1991. J. Geophys. Res. 103 (C9), 18567–18589 doi:10.1029/97JC01736.
Li, T., Wang, B., Chang, C.P., Zhang, Y., 2003. A theory for the Indian Ocean dipole–zonal mode. J. Atmos. Sci. 60 (17), 2119–2135.
Li, Y., Qiu, Y., Hu, J., Aung, C., Lin, X., Jing, C., Zhang, J., 2021. The strong upwelling event off the southern coast of Sri Lanka in 2013 and its relationship with Indian Ocean Dipole events. J. Clim. 34 (9), 1–51. https://doi.org/10.1175/JCLI-D-20-0620.1.
Liu, D., Duan, W., Feng, R., Tang, Y., 2018. "Summer Predictability Barrier" of Indian Ocean Dipole Events and Corresponding Error Growth Dynamics. JGR: Ocean 123. https://doi.org/10.1029/2017JC013739.
Lu, B., Ren, H., Scaife, A.A., Wu, J., Dunstone, N., Smith, D., Wan, J., Eade, R., Maclachlan, C., Gordon, M., 2018. An extreme negative Indian Ocean Dipole event in 2016: dynamics and predictability. Clim. Dyn. 51, 89–100.
Luo, J.J., Masson, S., Behera, S., Yamagata, T., 2007. Experimental forecasts of the Indian Ocean dipole using a coupled OAGCM. J. Clim. 20 (10), 2178–2190. https://doi.org/10.1175/JCLI4132.1.
Milly, P.C.D., Shmakin, A.B., 2002. Global modeling of land water and energy balances. Part I: The land dynamics (LaD) model. J. Hydrometeorol. 3 (3), 283–299.
Mu, M., Duan, W.S., 2003. A new approach to studying ENSO predictability: Conditional nonlinear optimal perturbation. Chin. Sci. Bull. 48, 747–749.
Mu, M., Feng, R., Duan, W.S., 2017. Relationship between optimal precursors for Indian Ocean Dipole events and optimally growing initial errors in its prediction. J. Geophys. Res. Oceans 122 doi:10.1002/2016JC012527.
Palmer, T.N., Gelaro, R., Barkmeijer, J., Buizza, R., 1998. Singular vectors, metrics, and adaptive observations. J. Atmos. Sci. 55, 633–653.

Qin, X., Duan, W.S., Chan, P.W., Chen, B., Huang, K.N., 2022. Effects of dropsonde data in field campaigns on forecasts of tropical cyclones over the western North Pacific in 2020 and role of CNOP sensitivity. Adv. Atmos. Sci. 40, 791–803. https://doi.org/10.1007/s00376-022-2136-9.
Qiu, Y., Cai, W.J., Guo, X.G., Ng, B., 2014. The asymmetric influence of the positive and negative IOD events on China's rainfall. Sci. Rep. 4, 4943.
Saji, N.H., Goswami, B.N., Vinayachandran, P.N., Yamagata, T., 1999. A dipole mode in the tropical Indian Ocean. Nature 401 (6751), 360–363.
Shi, L., Hendon, H.H., Alves, O., Luo, J.J., Balmaseda, M., Anderson, D., 2012. How predictable is the Indian Ocean dipole? Mon. Weather Rev. 140 (12), 3867–3884. https://doi.org/10.1175/MWR-D-12-00001.1.
Song, Q., Vecchi, G.A., Rosati, A.J., 2007. Indian Ocean Variability in the GFDL Coupled Climate Model. J. Clim. 20, 2895–2916. https://doi.org/10.1175/JCLI4159.1.
Stouffer, R.J., et al., 2006. GFDL's CM2 global coupled climate models. Part IV: Idealized climate response. J. Clim. 19, 723–740.
Szunyogh, I., Toth, Z., Majumdar, S., Morss, R., Etherton, B., Bishop, C., 2000. The effect of targeted observations during the 1999 Winter Storm Reconnaissance program. Mon. Wea. Rev. 128, 3520–3537.
Wajsowicz, R.C., 2004. Climate variability over the tropical Indian Ocean sector in the NSIPP seasonal forecast system. J. Clim. 17 (24), 4783–4804.
Wajsowicz, R.C., 2005. Potential predictability of tropical Indian Ocean SST anomalies. Geophys. Res. Lett. 32 (24), L24702. https://doi.org/10.1029/2005GL024169.
Wang, G., Cai, W., 2020. Two-year consecutive concurrences of positive Indian Ocean Dipole and Central Pacific El Niño preconditioned the 2019/2020 Australian "black summer" bushfires. Geosci. Lett. 7 (1). https://doi.org/10.1186/s40562-020-00168-2.
Webster, P.J., Moore, A.M., Loschnigg, J.P., Leben, R.R., 1999. Coupled ocean-atmosphere dynamics in the Indian Ocean during 1997-1998. Nature 401 (6751), 356–360.
Wittenberg, A.T., Rosati, A., Lau, N.C., Ploshay, J.J., 2006. GFDL's CM2 global coupled climate models. Part III: Tropical pacific climate and ENSO. J. Clim. 19 (5), 698–722. https://doi.org/10.1175/JCLI3631.1.
Xiao, F., Wang, D., Leung, M.Y., 2020. Early and extreme warming in the South China Sea during 2015/2016: role of an unusual Indian Ocean Dipole event. Geophys. Res. Lett. 47 (17). https://doi.org/10.1029/2020GL089936.
Yang, J.L., Liu, Q.Y., Liu, Z.Y., 2010. Linking observations of the Asian Monsoon to the Indian Ocean SST: possible roles of Indian Ocean basin mode and dipole mode. J. Clim. 23, 5889–5902.
Yu, Y., Mu, M., Duan, W.S., Gong, T., 2012. Contribution of the location and spatial pattern of initial error to uncertainties in El Niño predictions. J. Geophys. Res. 117, C06018. https://doi.org/10.1029/2011JC007758.
Yuan, D., Xu, P., Xu, T., 2017. Climate variability and predictability associated with the Indo-Pacific oceanic channel dynamics in the CCSM4 coupled system model. Chin. J. Oceanol. Limnol. 35 (1), 23–38.
Yuan, Y., Yang, H., Zhou, W., Li, C., 2008. Influences of the Indian Ocean dipole on the Asian summer monsoon in the following year. Int. J. Climatol. 28, 1849–1859.
Zhu, J., Huang, B., Kumar, A., Kinter, J.L., 2015. Seasonality in Prediction Skill and Predictable Pattern of Tropical Indian Ocean SST. J. Clim. 28 (20). https://doi.org/10.1175/JCLI-D-15-0067.1.